ELSEVIER

Journal of Nuclear Materials 277 (2000) 11–27

journal of nuclear materials

www.elsevier.nl/locate/jnucmat

Oxidation of β-Zr and related phases in Zr–Nb alloys: an electron microscopy investigation

Y.P. Lin[a,*], O.T. Woo[b]

[a] *Ontario Power Technologies, 800 Kipling Ave, Toronto, Ontario, Canada M8Z 6C4*
[b] *Atomic Energy of Canada Limited, Chalk River Laboratories, Chalk River, Ontario, Canada K0J 1J0*

Received 8 March 1999; accepted 17 June 1999

Abstract

The oxidation of the metastable β-Zr phase in Zr–Nb alloys, primarily Zr–2.5Nb, in 673 K steam or in lithiated water at 583 K, was investigated using electron microscopy and microanalyses. In the SEM, oxidised β-Zr regions in the Zr–2.5Nb alloy were imaged via a field effect contrast mechanism. In the TEM, microanalyses consistently showed the presence of Nb associated with the oxidised β-regions in suitably prepared samples. The β-Zr was found to form a $Nb_2Zr_{x-2}O_{2x+1}$ oxide, while the β-Nb exhibited delayed oxidation with respect to α-Zr, forming a metallic sub-oxide initially and becoming amorphous when oxidised. For the partially decomposed β-Zr, the ω-phase was found to form monoclinic ZrO_2, while the Nb-enriched β-Zr followed the behaviour of either β-Zr or β-Nb depending on the Nb concentration.

1. Introduction

Zirconium and its alloys are widely used in the nuclear industry. In CANDU reactors, Zr–2.5%Nb alloy is used as the material for pressure tubes. The microstructure of Zr–2.5Nb pressure tubes is highly anisotropic, due to extrusion near 1100 K followed by cold drawing. The microstructure consists of primarily elongated grains of hexagonal-close-packed α-Zr (<1%Nb), typically 0.3–0.5 μm thick. One feature that distinguishes this Zr–Nb alloy from other Zr alloys, such as the Zircaloys, is the presence of a metastable Nb-rich, body-centred-cubic (bcc) β-Zr phase, typically located at α-Zr grain boundaries and containing about 20%Nb. Below the monotectoid temperature (≈880 K), β-Zr will eventually transform to the equilibrium β-Nb phase (also bcc) containing about 85% or more of Nb.

Depending on the exposure condition, the transformation may involve the formation of an intermediate, Nb-depleted ω-phase with an associated Nb-enrichment in the surrounding β-Zr [1]. The pressure tubes are given a stress-relief treatment in steam at 673 K for 24 h as the last step of the manufacturing process. During this treatment, a protective oxide film is formed on the pressure tube surface while the β-Zr is partially transformed to the ω-phase and Nb-enriched β-Zr. Although most pressure tubes are produced this way, some developmental pressure tubes were given an additional heat treatment (prior to the treatment at 673 K) at 773 K for 6 h [2], during which the β-Zr is transformed to β-Nb with an associated change to a more discrete, particulate morphology.

Initially, the pressure tubes are installed with the oxide film formed during the stress-relief treatment. During service, this oxide film thickens due to a corrosion reaction with the coolant (lithiated heavy water) at typically between 520 and 570 K. The corrosion process and the concomitant pickup of a small amount of corrosion-released hydrogen or deuterium are of interest to the performance of the pressure tubes. Investigations of oxide microstructures are expected to contribute towards an improved understanding of these processes. There is thus a need to understand the oxidation of both the primary α-Zr phase and the secondary phases, namely the β-Zr in various states of decomposition. For

* Corresponding author. Tel.: +1-416 207 5986; fax: +1-416 236 0979.
E-mail address: yangpi.lin@oht.hydro.on.ca (Y.P. Lin).

0022-3115/00/$ - see front matter
PII: S0022-3115(99)00153-1

the α-Zr in Zr–2.5Nb, as in other Zr alloys, it is well established that the monoclinic form of ZrO_2, together with minor amounts of the tetragonal form of ZrO_2, is formed under a wide range of exposure conditions [3–6]. In comparison, not all aspects of the oxidation of the β-regions are well understood. A number of observations on the microstructure of oxides grown on Zr–2.5Nb alloy have been reported in recent years [6–14]. These works dealt with oxides formed in steam at 673 K [6–9,14] followed by re-exposure to 723 K vacuum or to gaseous environments at 573 or 600 K [7,8,10], or oxides grown in lithiated water at 523 [11] or 573 K [12,13]. Despite these reports, a consistent overall picture for the oxidation of the β-phases remains lacking, in part due to the state of β-Zr decomposition not being the primary focus. In addition, there appear to be uncertainties regarding the distribution of Nb in the oxide. Some works have shown the presence of Nb in oxidised β-Zr regions in oxides grown in water at 573 [13] or 673 K steam [14]. However, other works have reported an absence of Nb from the oxidised β-regions in oxides formed in 673 K steam [7] or in water at 523 K [11] and at 573 K [12], despite the occasional observation of significant amounts of Nb. Localisation of Nb was reported to occur upon re-exposure to reducing atmospheres at 723 K [7] or to CO_2-based gaseous environments at 600 K [10].

In the work described here, the oxides grown under different exposure environments on primarily Zr–2.5Nb pressure tube coupons have been investigated using electron microscopy and microanalysis. Emphasis is placed on the oxidised β-Zr and related regions, and attention is given to the state of the β-Zr prior to the corrosion exposure. In order to gain a more complete picture of the oxidation of the β-Zr and related phases, the work on Zr–2.5Nb materials is supplemented by work on a Zr–20Nb alloy, which has been annealed to simulate the behaviour of β-Zr.

2. Experimental

2.1. Materials

The Zr–2.5Nb material was taken from a standard production pressure tube. The composition based on ingot analysis is given in Table 1. The pressure tube used had not been subjected to a stress-relief treatment at 673 K and thus contained β-Zr in the undecomposed state. A section of the pressure tube material was subjected to a heat treatment of 6 h at 773 K to induce the transformation of β-Zr to β-Nb. Coupons approximately $20\times10\times1$ mm in dimension were prepared with their broad faces corresponding to the radial-normal section of the pressure tube. Prior to the oxidation, all coupons were chemically polished using a $HNO_3/H_2SO_4/HF/H_2O$ mixture. The oxides examined were grown either in steam at 673 K for 24 h or in steam followed by a re-exposure to lithiated water (pH 10.5) at 583 K for 176 days; the initial steam exposure was at 673 K for either 24 or 350 h.

The Zr–20Nb alloy used was annealed at 1123 K for 1 h and air-cooled to produce a single-phase β-Zr structure. The composition based on ingot analysis is given in Table 1. Prior to the oxide forming exposure, coupons were chemically polished using a $HNO_3/H_2SO_4/HF/H_2O$ mixture. Coupons were exposed to either lithiated water at 573 K for three days or exposed to air at 673 K for 2 h. The alloy was also aged at 773 K for 1000 h to produce an equilibrium structure of α-Zr + β-Nb. The aged alloy was exposed to lithiated water at 573 K for 76 days.

2.2. Electron microscopy

Scanning electron microscope (SEM) examination was carried out using a JEOL 840 machine operated at 3–10 keV. The oxide samples were examined, without the application of a conductive surface coating, using a conventional Everhart–Thornley secondary electron detector and a segmented backscattered electron detector. The backscattered electron detector was used to provide images based on topographical or compositional contrast. The Everhart–Thornley secondary electron detector was operated in three modes. In the first, the bias voltage on the cage of the detector was maintained to provide conventional secondary electron images. In the second, the bias voltage was switched-off, such that only limited secondary electrons formed the image. This mode is termed the no-bias mode. In the third, the bias voltage is reversed to image only backscattered electrons.

For examination in the transmission electron microscope (TEM), plan-view and cross-sectional oxide foils were prepared. For plan-view foils, 3 mm discs were prepared from the corrosion coupons. The discs were mechanically thinned from the metal side to a thickness of between 100 and 150 μm. The metal at the central

Table 1
Compositions of Zr–2.5Nb pressure tube material and Zr–20Nb alloy used, based on ingot analysis

Nb (wt%)	O (ppm)	C (ppm)	Fe (ppm)	N (ppm)	Si (ppm)	Zr
2.5	1130	145	430	34	<60	Balance
20.0	1200	60	440	22	<25	Balance

portion of the disc was then dished either chemically using a $HNO_3/H_2SO_4/HF/H_2O$ mixture or by electropolishing at 233 K with a perchloric acid/methanol electrolyte. Final thinning to electron transparency was achieved using an ion-mill operated with Ar^+ ions at between 4 and 6 kV. A single ion beam was used. When the beam was directed at the outer surface of the oxide, the resultant electron transparent foil was located at the interfacial region of the oxide. When the beam was directed at the metal side, the electron transparent foil was located at the surface region of the oxide. Cross-sectional foils were prepared by first gluing together two pieces of oxide films. The composite was cut and mechanically thinned, then dimpled and finally ion-milled to perforation. Foils of the bulk alloy were prepared by electropolishing using a perchloric acid/methanol electrolyte at 233 K. The thin foils were examined in a JEOL 2010 TEM operated at 200 keV or in a Philips CM30 TEM operated at 300 keV. Both instruments are equipped with an Oxford Instrument energy dispersive X-ray (EDX) spectroscopy system. The EDX detectors are of the ultra-thin window type and are capable of detecting light elements. For electron energy loss spectroscopy (EELS) analyses, Gatan parallel detection systems attached to the CM30 TEM and a JEOL 2010F TEM were used.

2.3. Assessment of oxygen content

One objective of EDX analysis was to assess the oxygen content in the Nb-containing regions in the oxide. However, the comparison of oxygen concentrations based on relative peak heights in EDX spectra is complicated by the low energy O–K X-rays being highly susceptible to absorption due to sample thickness. In principle, absorption can be addressed if the composition, or more strictly, the density, of the analysed region is known. For ZrO_2, which has a limited range of stoichiometry, a link was previously established between the observed O–K-to-Zr-K_α ratio and the local foil thickness [14]. The local foil thickness was estimated from the count rate of the Zr-K_α X-rays normalised by the probe current. This method of foil thickness determination was verified against measurements made using convergent beam electron diffraction (CBED) [14]. For the EDX detector attached to the JEOL 2010 TEM, the ZrO_2 foil thickness (in nanometer) can be derived from the normalised Zr-K_α count rate (in counts per second per nanoampere) by a multiplication factor of 0.185. For the analyses of Nb-enriched regions in the oxide, the thickness of the analysed region is an unknown parameter. However, it may be assumed that the thickness would be within the range of the thickness of the surrounding ZrO_2. Additional measurements were therefore made on several ZrO_2 locations adjacent to each Nb-enriched region analysed. The observed ratio of the O–K-to-(Zr-K_α + Nb-K_α) X-ray counts was then plotted against the normalised count rate of the metal-K_α X-rays. Assuming comparable local thickness, the plot was then interpreted with the understanding that the level of absorption of the low energy O–K X-rays from the Nb-enriched region was comparable with that from the adjacent ZrO_2.

3. Results

3.1. β-Zr prior to oxidation

Two types of materials that contained β-Zr in the undecomposed state prior to corrosion exposures were investigated. The first is the cold-drawn Zr–2.5Nb pressure tube material that had not been exposed to a stress-relief treatment at 673 K. The second type is a Zr–20Nb alloy containing single-phase β-Zr produced by air-cooling after annealing at 1123 K for 1 h.

3.1.1. Oxidised β-Zr in Zr–2.5Nb

Some unusual SEM image contrasts were observed on the surfaces of the oxides grown on polished Zr–2.5Nb pressure tube coupons. Some decomposition of the β-Zr was expected during the oxide-forming exposure in 673 K steam (for various times up to 24 h). However, as the oxide growth was inwards, the examined surface corresponded to regions containing undecomposed β-Zr. The secondary electron image contrast was found to vary with the settings of the Everhart–Thornley detector. The optimum feature contrast was obtained when the bias voltage on the detector was switched off, i.e. in the no-bias mode, Fig. 1(a)–(d). Imaging using backscattered electrons did not reveal significant contrast [15], indicating that the image contrast in Fig. 1 was not due to compositional or topographical variations.

A striking characteristic of this type of image contrast was the variation of feature size with accelerating voltage. Fig. 1(a)–(d) show images of the same area examined at 3, 5, 7 and 9 keV, respectively for a 0.8 μm thick oxide. At the lowest accelerating voltage, 3 keV, Fig. 1(a), the observed features were narrow and elongated. As the accelerating voltage was increased, the size and the area fraction of the features increased. The correlation between the features at different accelerating voltages was self evident at low voltages, Fig. 1(a) and (b), but became less evident at higher voltages as the features merged into each other. The dependency of the feature size on the accelerating voltage implied that the contrast was related to the penetration depth of the incident electrons. As secondary electrons generally provide information on surface topography, a voltage dependency of the secondary electron image was rather unusual.

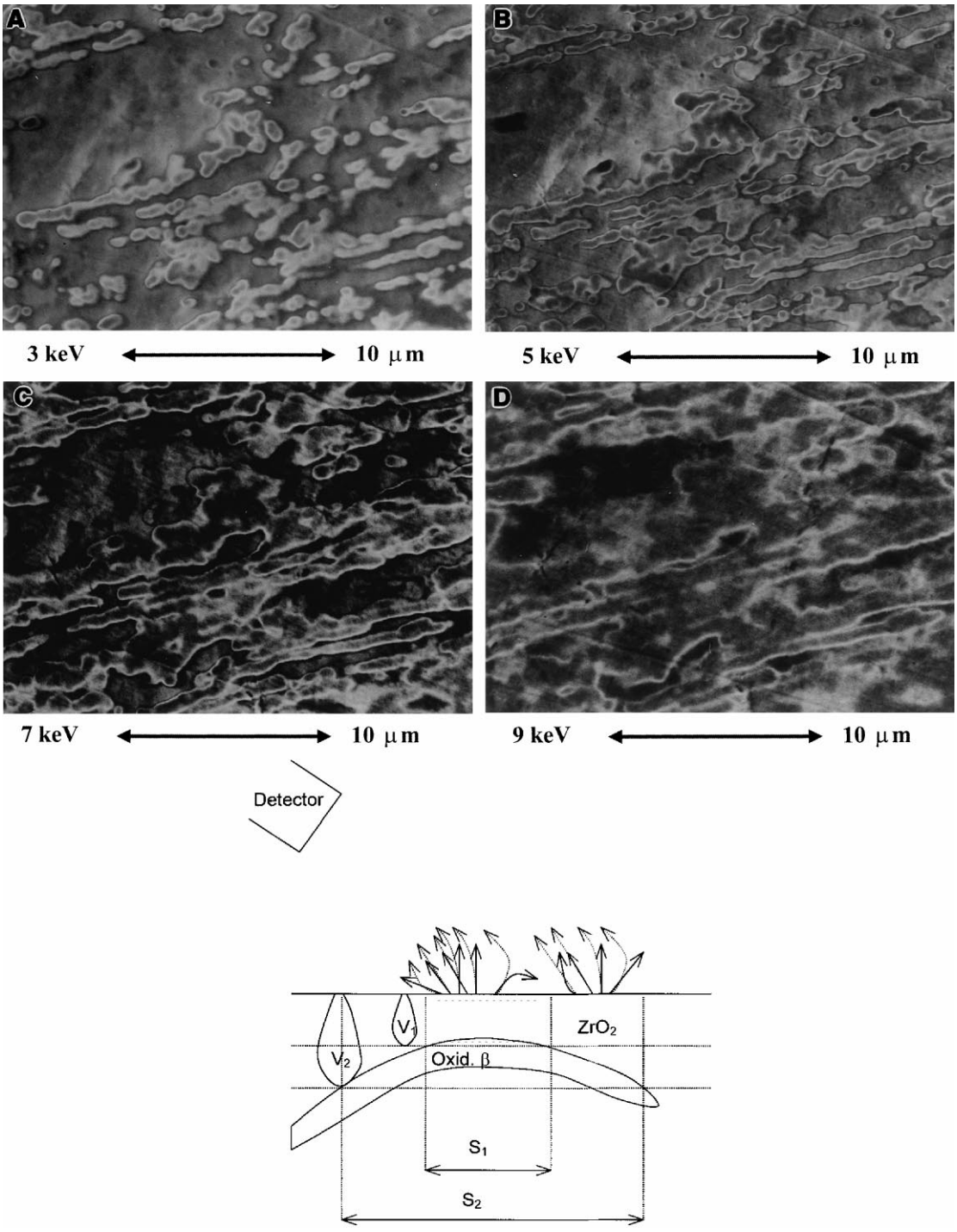

Fig. 1. SEM micrographs of Zr–2.5Nb pressure tube oxide formed in 673 K steam and imaged in the no-bias mode at: (a) 3 keV, (b) 5 keV, (c) 7 keV, (d) 9 keV accelerating voltages and (e) schematic diagram showing the interaction of electron beam with oxidised Zr–2.5Nb. The efficiency of secondary electron collection is increased when a bias voltage is applied to the detector (dotted trajectories). V_1 and V_2 are interaction volumes at accelerating voltages E_1 and E_2 ($E_1 < E_2$). Transfer of charge to sample surface is established by beam induced conductivity. The apparent feature sizes, S_1 and S_2, are dependent on the accelerating voltage and the morphology of oxidised β-Zr.

The origin of the contrast can be attributed on several counts to the oxidised β-Zr phase in the oxide. First, un-etched coupons of Zr–2.5Nb alloy did not reveal such a contrast, indicating that the contrast was a property of the oxide film. Second, oxides of Zircaloy-2 similarly formed under 673 K steam did not reveal such a contrast, indicating that the contrast was not simply associated with the ZrO_2 oxidised from α-Zr but was specific to the oxides containing β-Zr. Third, the features observed at low voltages resembled the β-Zr morphology, Fig. 1(a) and (b).

This ability to reveal the microstructure beneath the sample surface was applied to the examination of the outer surface of an as-manufactured Zr–2.5Nb pressure tube, which contained an oxide formed during the stress-relief treatment at 673 K in steam. Fig. 2 shows that features corresponding to oxidised β-Zr can be readily observed. Compared with the oxide formed on polished coupons shown in Fig. 1(a)–(d), the oxidised β-Zr on the as-manufactured tube, Fig. 2, was more discontinuous and had suffered certain degree of smearing. Such an effect is consistent with the machined finish on the outer surface of the pressure tube.

The main implication arising from the above observations is that the oxidised β-Zr has a different response to the incident electrons in the SEM compared with the surrounding oxide formed from α-Zr. It follows that there are structural and compositional differences between the oxidised β-Zr and ZrO_2 oxidised from α-Zr.

3.1.2. Oxidised β-Zr in Zr–20Nb

The structure of the oxide grown on β-Zr was investigated using a Zr–20Nb alloy that was initially in the single-phase form (β-Zr) produced by air-cooling from the annealing temperature at 1123 K. For such material oxidised in 573 K water or in air at 673 K, previous Raman spectroscopy results suggested a nearly cubic structure based on comparisons with the cubic and tetragonal polymorphs of ZrO_2 [16]. Subsequent investigation showed that such a description was inadequate [17]. TEM showed that this oxide was characterised by the presence of microdomains, Fig. 3(a), and complex selected area diffraction (SAD) patterns, Fig. 3(b). Analysis of SAD and additional CBED patterns, Fig. 3(c), showed that the oxide structure is consistent with an incommensurate superstructure oxide $Nb_2Zr_{x-2}O_{2x+1}$ reported by Thompson, Withers and co-workers for $x = 7.1$–12.0 [18–20]. According to these workers, $Nb_2Zr_{x-2}O_{2x+1}$ oxide can be thought of as a superstructure derived from orthorhombic subcells of metal and oxygen atoms that have slightly mismatched dimensions [18–20]. The superstructure is x times larger in one direction than the metal subcell, such that x metal subcells accommodated $2x + 1$ oxygen subcells. In essence, more oxygen atoms are being accommodated due to the higher valence of Nb.

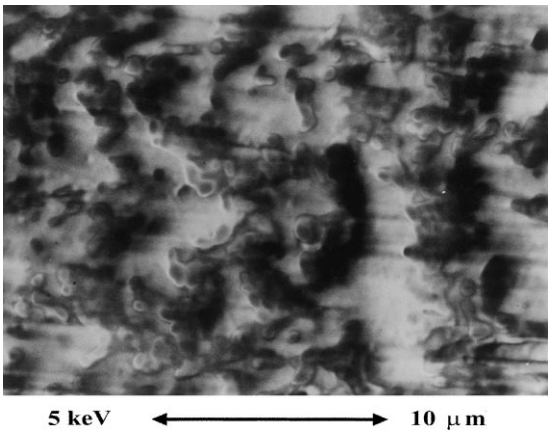

Fig. 2. SEM image at 5 keV taken from the outside surface of a Zr–2.5Nb pressure tube.

For the present Zr–20Nb oxide, the metal subcell dimensions, determined from the strong reflections in diffraction patterns were $a = 0.52$, $b = 0.50$ and $c = 0.53$ nm, in reasonable agreement with those reported for $Nb_2Zr_{x-2}O_{2x+1}$ with $x = 10$ [18]. A value of 9.5 ± 0.3 for x was estimated from high resolution images and from the spacing of satellite reflections in SAD patterns [17]. The estimated value of x is slightly lower than a value of 10.15 expected for a 20 wt% Nb composition, attributed to an increase in Nb concentration from the decomposition of β-Zr.

3.2. Oxidised β-Nb

Two types of materials containing β-Nb prior to corrosion exposures were examined. The first type was the Zr–2.5Nb pressure tube material that had been heat-treated for 6 h at 773 K. The second was a Zr–20Nb alloy that had been annealed at 1123 K and aged for 1000 h at 773 K.

In the Zr–2.5Nb material, two types of Nb-enriched regions in the oxide have been identified, depending on the location relative to the interface with the metal. Crystalline Nb-enriched regions were observed close to the interface, while amorphous Nb-enriched regions were observed away from the interface. The variation with location is illustrated in Fig. 4(a), taken from the mid-portion of a cross-sectional foil of a ≈0.8 μm thick oxide formed in 673 K steam. In Fig. 4(a), a crystalline region is indicated by the arrow marked as **S** and an amorphous region is indicated by the arrow marked as **A**.

Similar crystalline and amorphous Nb-enriched regions were observed in oxides grown in 583 K lithiated (pH 10.5) water for a total of 176 days following an initial exposure to 673 K steam for 24 h. Fig. 4(b) shows a region in a plan-view foil prepared such that

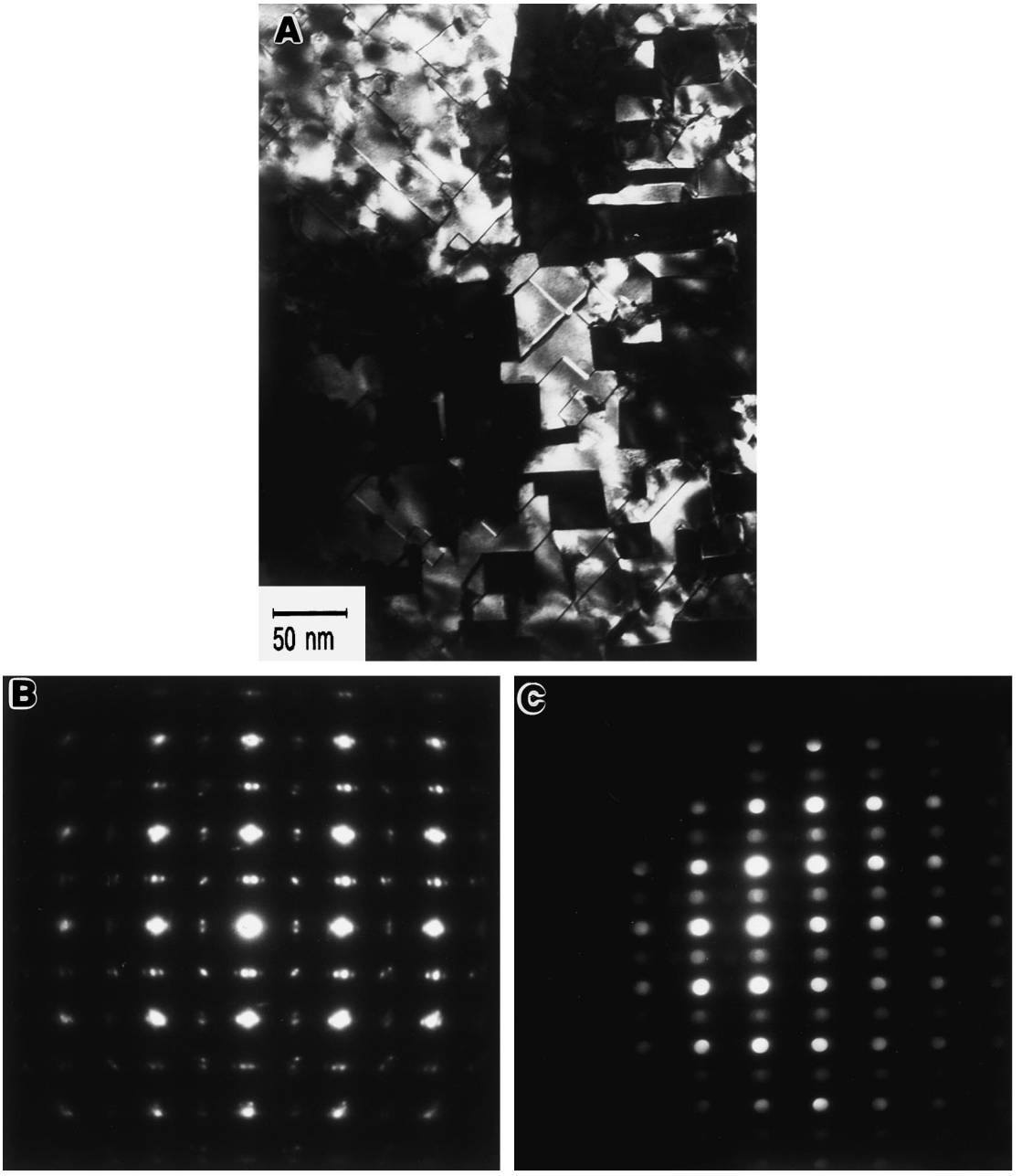

Fig. 3. (a) Dark field TEM image showing a domain structure of multiple orientations in a 673 K air-formed oxide of single phase Zr–20Nb alloy (plan-view foil). (b) Selected area diffraction pattern showing a complex array of strong and weak reflections. (c) Convergent beam electron diffraction pattern from one variant of the Zr–20Nb oxide; the pattern is consistent with $Nb_2Zr_{x-2}O_{2x+1}$, ($x = 9.5$).

the examined oxide was located immediately adjacent to the interface with the metal. The positions of Nb-enriched regions were not immediately apparent in the image but were apparent in the Nb EDX map, Fig. 4(c). Close examination of the area showed that many of the Nb-rich regions overlapped with ZrO_2 grains. However, the central portion of Fig. 4(b) and (c) was free of the overlapping problem. When the same oxide was prepared such that the examined oxide corresponded to the outer oxide surface, amorphous Nb-enriched regions were observed as shown in Fig. 4(d).

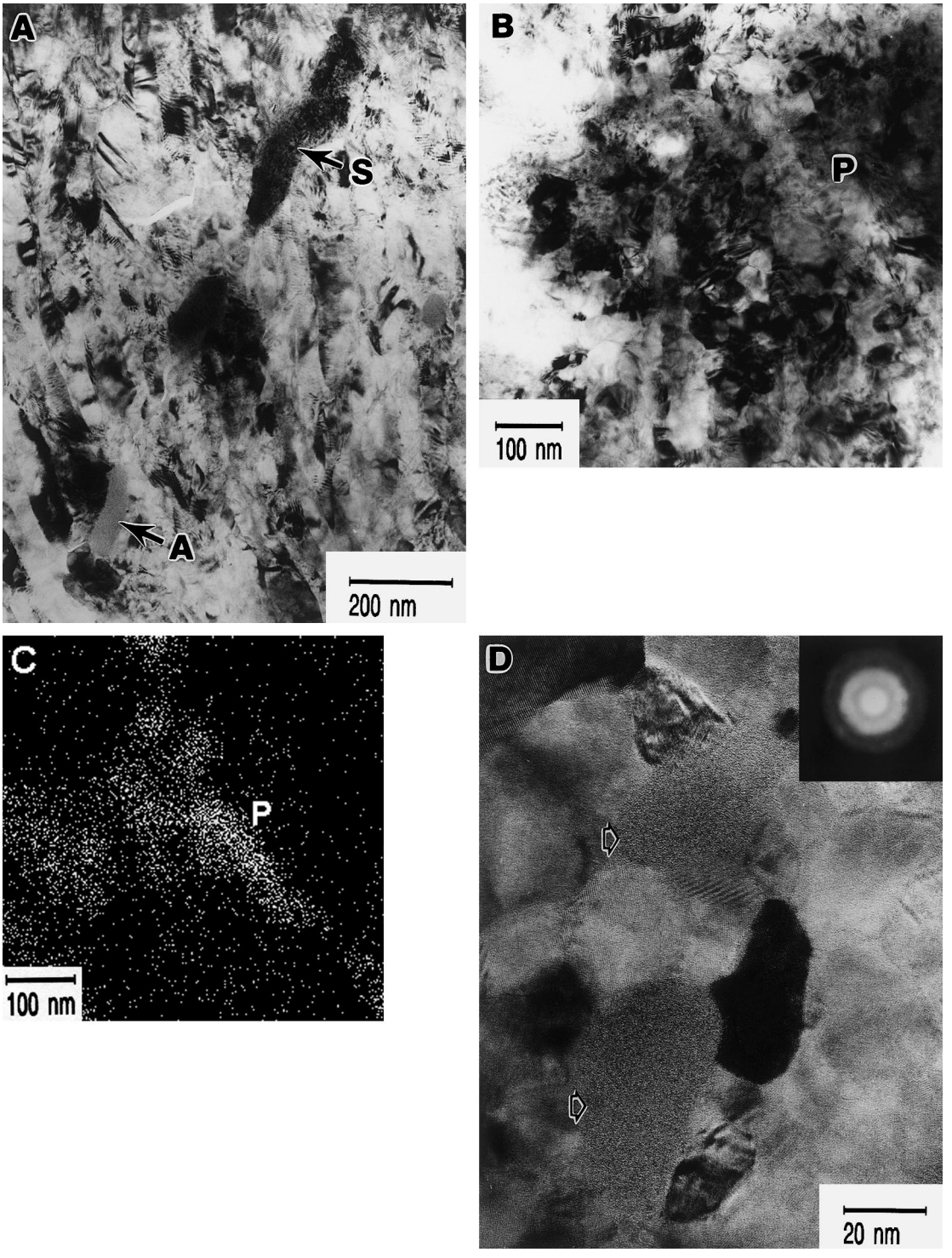

Fig. 4. (a) Crystalline sub-oxide (arrow marked **S**) and amorphous Nb oxide (arrow marked **A**) in a cross-sectional TEM foil of a Zr–2.5Nb oxide formed in 673 K steam. (b) Region in a plan-view TEM foil prepared such that the oxide examined was located immediately adjacent to the metal interface. The Zr–2.5Nb sample was heat-treated at 773 K prior to oxide-forming exposures. The oxide was formed by exposures to steam at 673 K for 24 h followed by lithiated water at 583 K for 176 days. (c) Nb-K_α X-ray map for the area shown in (b). **P** marks the same location in (b) and (c). (d) Amorphous, Nb-enriched oxide located near the outer surface of the same oxide as in (b); insert shows diffuse rings in the diffraction pattern from the amorphous region.

The Nb concentrations in the crystalline regions were high, Fig. 5(a), similar to those in the β-Nb in the metal. The lower oxygen concentration relative to the surrounding ZrO_2, Fig. 5(a), was confirmed by plotting the ratio of the O–K to metal-K_α X-ray counts against the count rate of the metal-K_α X-rays normalised by the probe current. As stated in Section 2, such a comparative plot provides an improved confidence to the assessment of the local oxygen content. In Fig. 5(b), the normalised count rate of the metal (Zr-K_α + Nb-K_α) X-rays from the crystalline region was outside the range of the surrounding ZrO_2. Since the physical thickness of the crystalline region was expected to be within the range of the surrounding ZrO_2, this high normalised count rate implied a substantially higher density of metal atoms. The comparison in Fig. 5(b) shows that the low oxygen-to-metal stoichiometry in the crystalline region is significant and is not likely the result of foil thickness variation, but is associated with a high density of metal atoms. The EDX results thus indicate that the

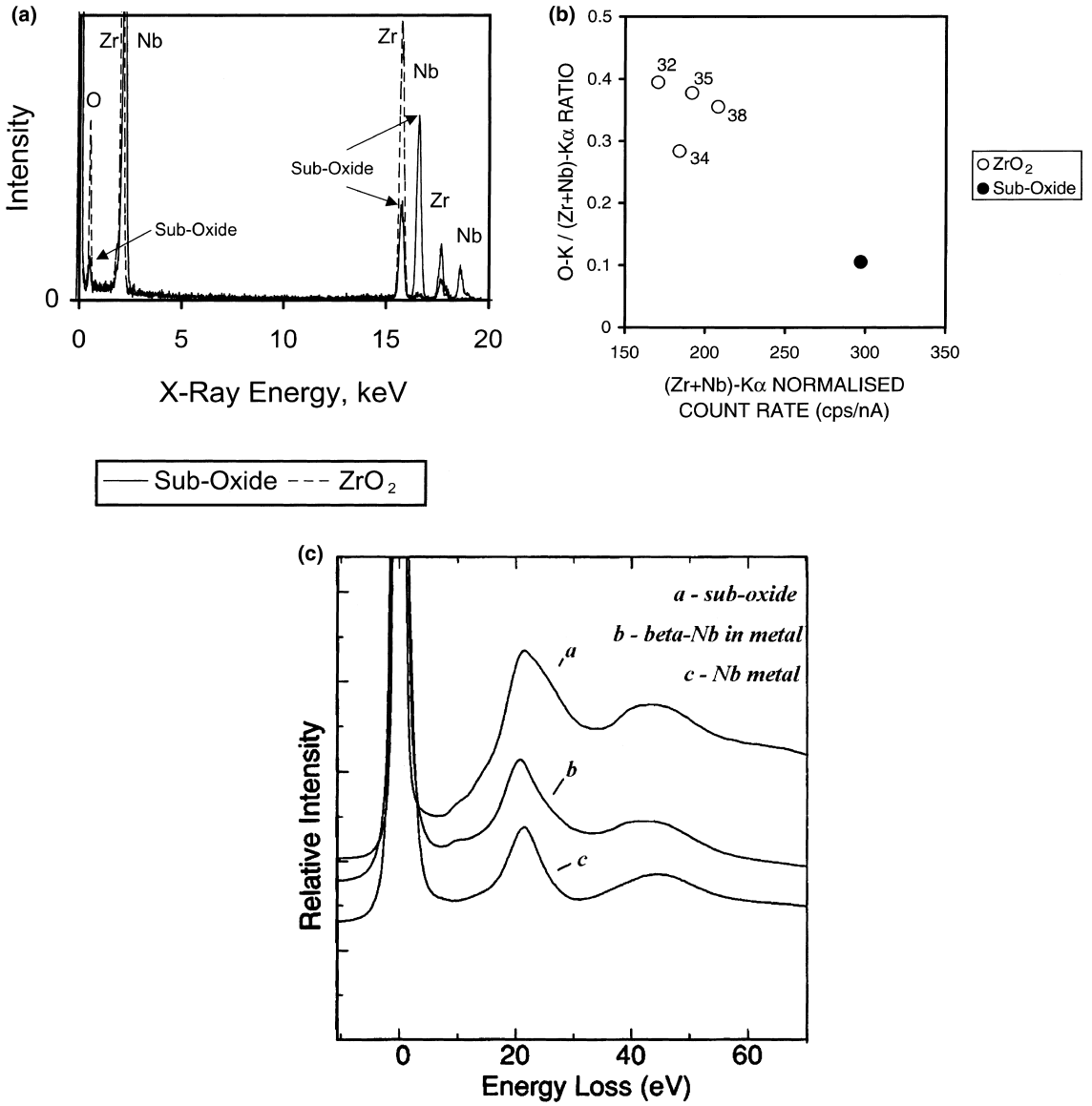

Fig. 5. (a) EDX spectra showing high Nb and low O contents in the sub-oxide compared with adjacent ZrO_2. (b) Plot of O–K/(Zr-K_α + Nb-K_α) ratio versus normalised (Zr-K_α + Nb-K_α) count rates for the sub-oxide and adjacent ZrO_2. The equivalent thickness in nanometer for ZrO_2 is given. (c) Comparison of the low loss region of EELS spectra acquired from the sub-oxide, the β-Nb in the metal and a Nb sample.

oxidation of the Nb-enriched crystalline region was incomplete.

A low loss EELS spectrum acquired from the crystalline Nb-enriched region in the oxide is shown in Fig. 5(c) together with similar spectra from the β-Nb in the metal and from a Nb foil. The spectra are similar – each spectrum consists of a single plasmon peak at near 21 eV and a broad Nb $N_{2,3}$ edge at around 43 eV. The slight variation in the peak location amongst the spectra may be due to the presence of some O and/or Zr. For the present purpose, it is pertinent to note the presence of a single plasmon peak. For the metallic Nb and β-Nb, as for metals in general, the plasmon peak is associated primarily with the excitation of free electrons [21]. The presence of a single plasmon peak in the spectra from the crystalline Nb-enriched region in the oxide indicates that the region was metallic in nature. This observation is particularly significant when compared with the EELS results obtained from amorphous Nb-rich regions presented below.

The microdiffraction patterns obtained from these crystalline Nb-rich regions in the oxide were consistent with a body-centred-tetragonal structure with $a = 0.33$ and $c = 0.35$ nm [14]. These parameters are similar to that of 0.336 nm for the bcc β-Nb (≈85%Nb). The structure of the crystalline Nb-rich regions can be thus regarded as a distortion of β-Nb due to the incorporation of dissolved oxygen. Such a structure based on the distortion of a parent bcc lattice shares similarities with the phase Nb_6O, observed for niobium oxidised between 573 and 773 K [22,23]. The difference in the actual values of lattice parameters may be accounted for by the presence of ≈15% Zr in β-Nb.

The EDX, EELS and diffraction information thus collectively identify the crystalline Nb-enriched regions in the oxide as a sub-oxide of β-Nb. The term sub-oxide is used here to mean that the phase is distinct from the parent β-Nb phase and that, despite the incorporation of some oxygen, the phase is primarily metallic in nature.

A second type of oxidised Nb-enriched regions in the Zr–2.5Nb material was the amorphous region located away from the growth interface, Figs. 4(a) and (d). The amorphous nature was evident from the typical speckled contrast, which did not change with the sample tilt, and from microdiffraction patterns that were dominated by diffuse rings. EDX analyses showed that the Nb concentration was comparable with that of the β-Nb in the metal. Fig. 6(a) shows that the oxygen concentration in the amorphous region was comparable with that of the surrounding ZrO_2. Since these amorphous regions were observed in the older (outer) parts of the oxide, the present results indicate that amorphisation was the result of the oxidation of the β-Nb or its sub-oxide.

Similar Nb-enriched amorphous regions were observed in oxides grown on the aged Zr–20Nb alloy that contained β-Nb prior to oxidation. The microstructure of this aged Zr–20Nb alloy consisted of equiaxed grains of β-Nb distributed in a matrix of α-Zr grains. An oxide region taken from a cross-sectional TEM foil prepared from a ≈20 μm thick oxide formed in oxygenated water at 573 K is shown in Fig. 7(a). The micrograph shows the presence of localised amorphous regions, the size of which resembled that of β-Nb in the metal. The corresponding EDX spectrum confirming high Nb and oxygen concentrations is shown in Fig. 7(b).

The nature of the amorphous Nb-enriched regions compared with powders of Nb_2O_5 was investigated using EELS. Fig. 6(b) shows that the low loss region of the spectrum from the amorphous region closely resembled that from Nb_2O_5. Above about 35 eV, both spectra in Fig. 6(b) exhibit a strong peak at near 45 eV with a minor peak or plateau at near 40 eV. These features can be compared with a single broad peak centred near 43 eV for the sub-oxide or β-Nb shown in Fig. 5(c). Of significance is the region between 10–30 eV loss. The spectra in Fig. 6(b) show two overlapping peaks located at about 15 and 26 eV. Similar double peaks at 14 and 26 eV were observed for ZrO_2, Fig. 6(b). In a previous EELS investigation of ZrO_2, these peaks were attributed to the splitting of energy levels within the valance and conduction bands of the oxide [24], i.e. these peaks are the consequence of the non-metallic nature of metal-oxygen bonds. The double peaks in Fig. 6(b) for the Nb_2O_5 and the amorphous regions are interpreted in a similar manner and are taken to be characteristic of a non-metallic compound, in this case an oxide. The double peaks for the amorphous regions can be contrasted with the single plasmon peak (near 21 eV in Fig. 5(c)) that is typical of excitation of free electrons in metals and alloys. The present EELS data thus show that, while the β-Nb sub-oxide remained metallic in nature, the amorphous Nb-enriched material was an oxide of β-Nb.

3.3. Oxidation of partially decomposed β-Zr

Materials containing the ω-phase and the Nb-enriched β-Zr prior to oxidation include those that have been heat-treated prior to the corrosion exposure and those that have undergone partial decomposition during the corrosion exposure. This type of material is important with respect to reactor operation conditions, where the ω + Nb-enriched β-Zr microstructure may persist longer than in the absence of irradiation [25]. TEM foils of oxides of Zr–2.5Nb, in either cross-section or plan-view orientations, have been examined. In the case of materials that have not received a heat treatment prior to the corrosion exposure, attention was placed on plan-view foils prepared from the interfacial region of a given oxide or on locations away from the surface in cross-section foils.

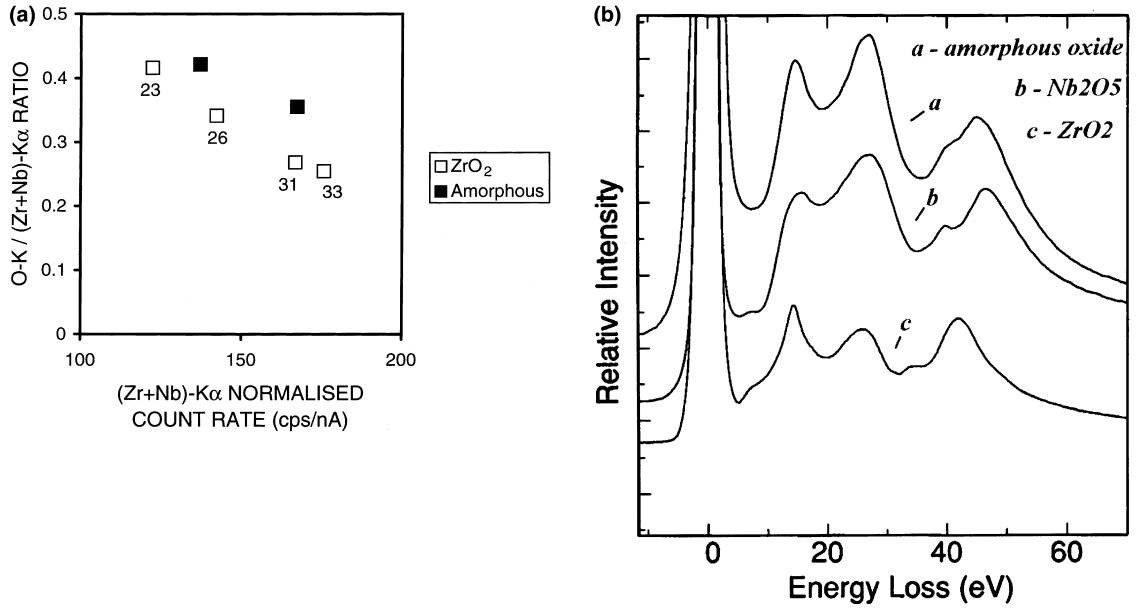

Fig. 6. (a) Plot of O–K/(Zr-K_α + Nb-K_α) ratio versus normalised (Zr-K_α + Nb-K_α) count rates for the amorphous, Nb-enriched region and the adjacent ZrO_2. The equivalent thickness in nanometer for ZrO_2 is given. (b) Low loss region of EELS spectra acquired from an amorphous, Nb-enriched region and a sample of Nb_2O_5; for comparison, a spectrum from ZrO_2 is included.

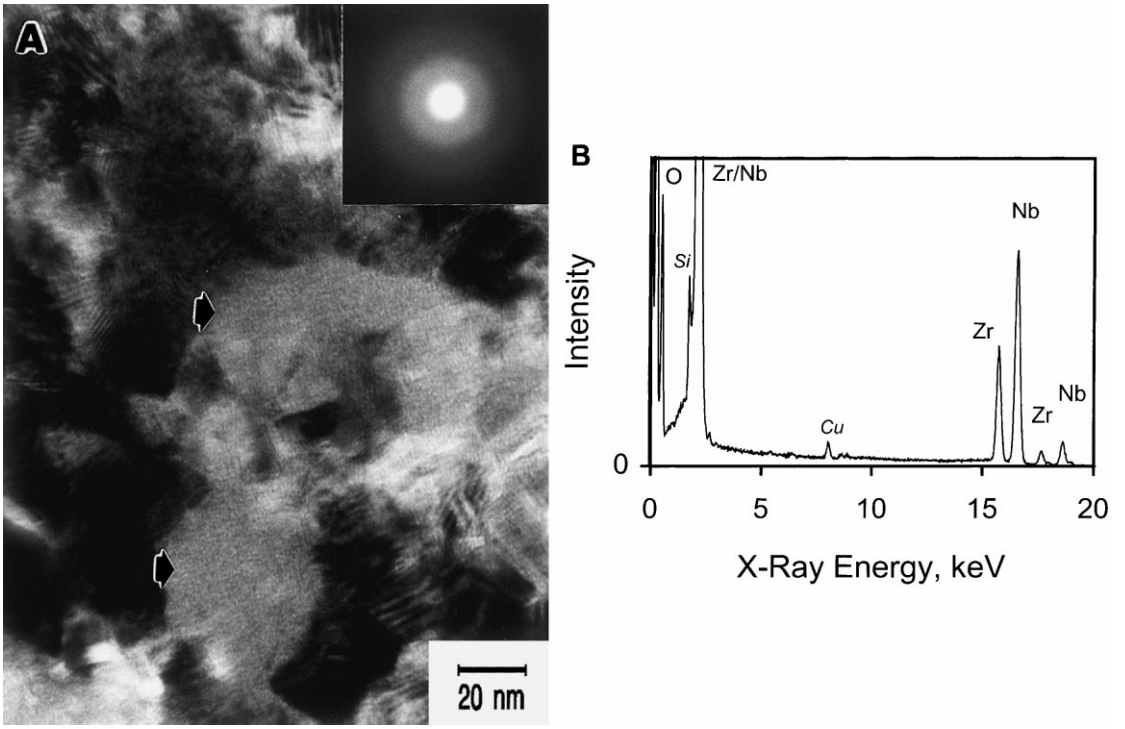

Fig. 7. (a) TEM micrograph of an oxide formed from an aged Zr–20Nb alloy, showing amorphous oxidised β-Nb regions; insert shows diffuse rings in the diffraction pattern from the amorphous region. (b) EDX spectrum from the amorphous region, showing high Nb and O contents (the Si and Cu signals are from the assembly used to produce the cross-section TEM foil).

A region containing oxidised β-Zr in a 673 K steam-formed oxide in Zr–2.5Nb oxide is shown in Fig. 8(a). Similar regions were identified in oxides grown in 583 K lithiated water. The interface between the oxidised β-Zr region and the surrounding ZrO_2 was found to be often decorated by pores, Fig. 8(a). The Nb concentration within the oxidised β-Zr region (without distinguishing between the ω-phase and the Nb-enriched β-Zr) detected using EDX was comparable with that in the β-Zr in the metal. Using a small focused probe (7 nm or less), the observed Nb concentration was often variable, depending on the size and placement of the focused probe. Nb

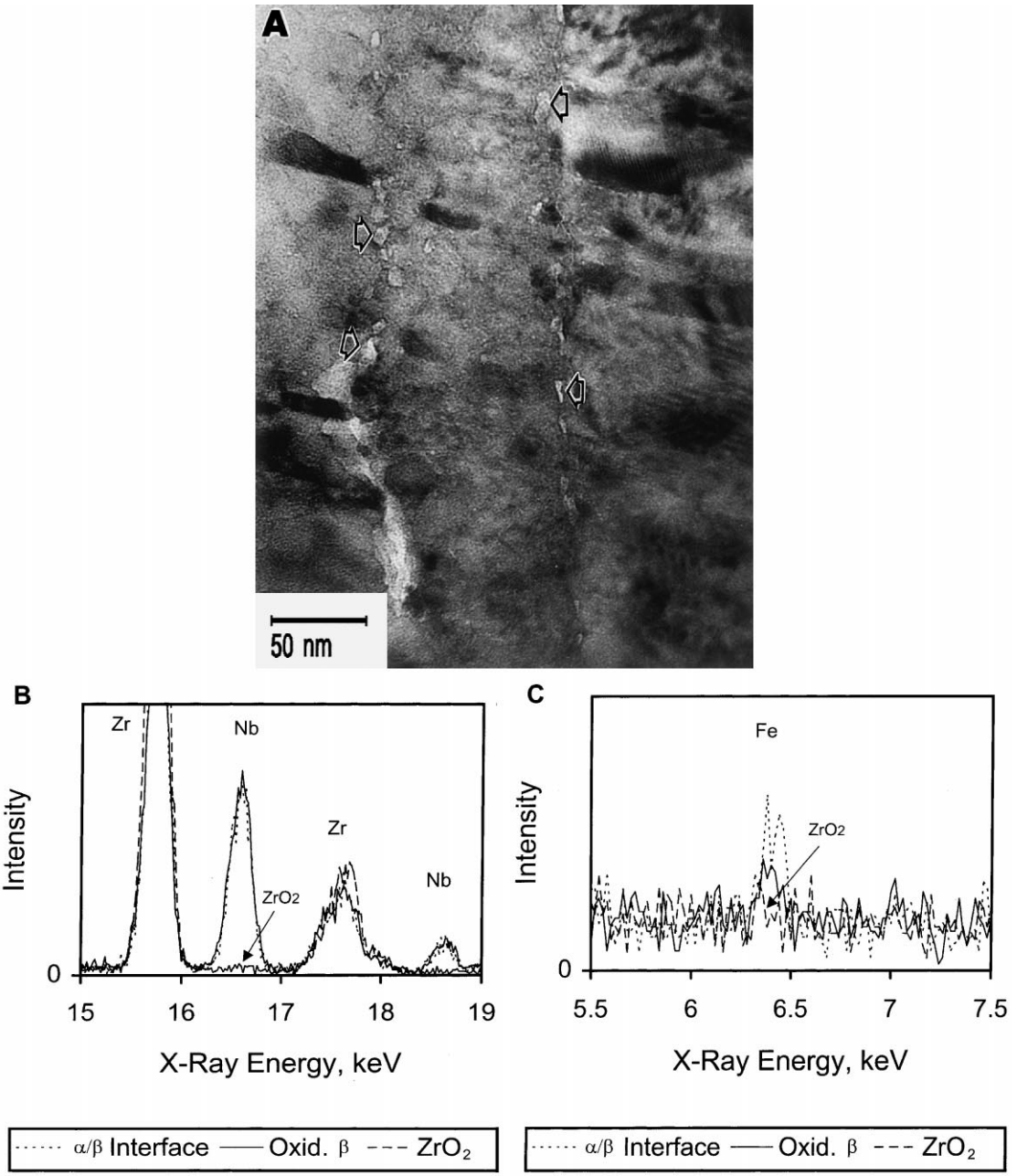

Fig. 8. (a) Image of an oxidised β-Zr band in a cross-sectional TEM foil of a Zr–2.5Nb oxide. Arrows indicate some interfacial pores. (b) and (c) EDX spectra showing presence of Nb (b) and Fe (c) at the interface between oxidised α-Zr and β-Zr; adjacent ZrO_2 exhibits low Nb and Fe, while adjacent oxidised β-Zr shows high Nb but lower Fe.

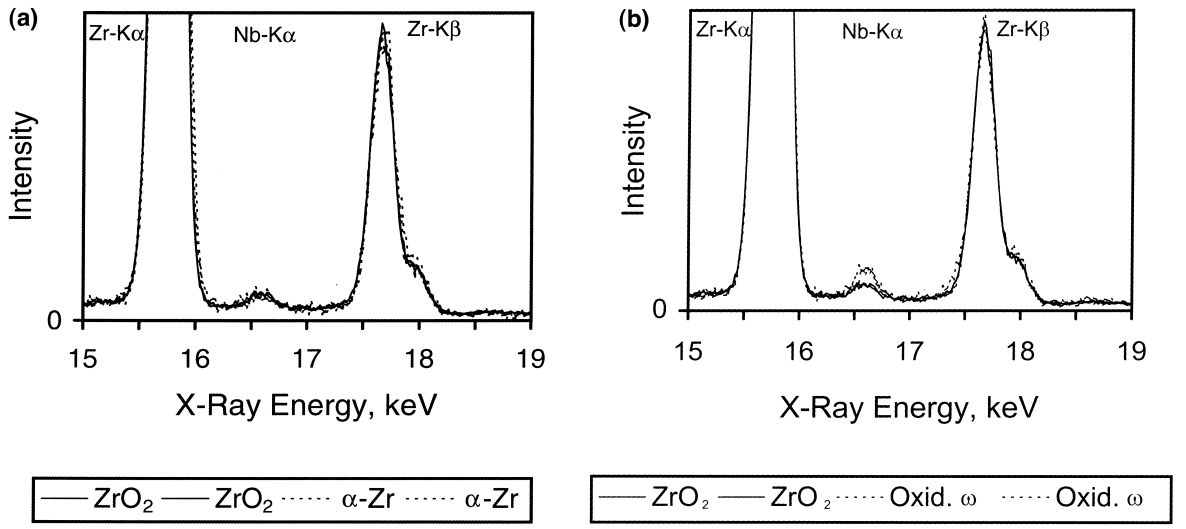

Fig. 9. Zr-K and Nb-K region of EDS spectra from the interfacial regions of an oxide formed during exposures to 350 h at 673 K followed by 176 days at 583 K: (a) Comparison showing similarity between the ZrO_2 and the α-Zr in the AR condition. (b) Comparison showing slightly higher Nb in the oxidised ω than in the surrounding ZrO_2. Two spectra from each location are shown. All spectra are scaled to the same Zr-K_α intensity.

concentrations higher than ≈20% for the undecomposed (and unoxidised) β-Zr were sometimes observed. Such observations are consistent with the partial decomposition of β-Zr. A location that consistently yielded a significant amount of Nb was the interface between the oxidised α-Zr and β-Zr. The example in Fig. 8(b) shows that the Nb concentration within the oxidised β-Zr and at the interface between oxidised β-Zr and α-Zr was significantly higher than those in the adjacent ZrO_2.

While a significant amount of Nb was present in the oxidised β-regions, the complementary Nb concentration in the ZrO_2 oxidised from α-Zr was generally low, Figs. 8(b) and Fig. 5(a). A comparison of the Nb concentration in the α-Zr metal and in the ZrO_2 is shown in Fig. 9(a). In this comparison, the α-Zr was from a Zr–2.5Nb pressure tube material in the as-received condition and the ZrO_2 was from an oxide (the interfacial region) grown in steam at 673 K for 350 h followed by re-exposure to lithiated water at 583 K for 176 days. The results show that the Nb concentration was not significantly affected by the oxidation of α-Zr into ZrO_2. The Nb concentrations in the ZrO_2 and in the α-Zr were 0.6–0.7 wt%, in accord with previous EDX measurements on Zr–2.5Nb pressure tube materials [26,27] and with the maximum solubility for Nb in α-Zr [28].

It is worth noting that in foils of Zr–Nb oxides, the locations of the oxidised β-regions may not be always immediately apparent, for example, see Fig. 4(b). The difficulty is related in part to the lack of a suitable contrast mechanism based on composition; Zr and Nb being adjacent elements in the periodic table. The

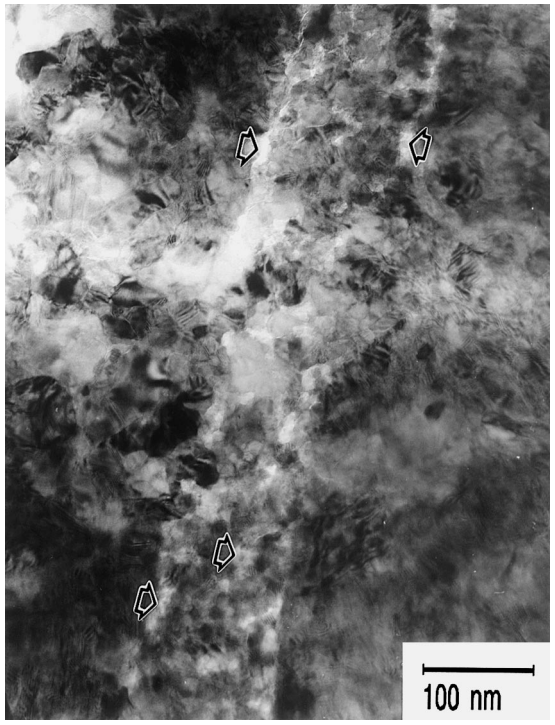

Fig. 10. TEM image (plan-view) of oxidised ω-phase in an interfacial region of an oxide formed in lithiated water for 176 days at 583 K following exposure for 350 h at 673 K in steam. Some pores introduced by the chemical removal of the metal are indicated by arrows.

oxidised β-regions usually can be located by observing the image contrast variation as the oxide foil was tilted in the TEM. However, the fine grain size of the ZrO_2 meant that diffraction conditions that would bring out contrast from the oxidised β-regions could not be consistently selected. Although EDX mapping could be used to locate the Nb-enriched regions, imaging of the region still required an appropriate diffraction contrast condition. Nevertheless, once identified, the presence of Nb was readily detected. The only exception encountered was in plan-view foils that were prepared using a chemical polish (rather than electropolish) to remove the metal and the final electron transparent region came from the interfacial region of the oxide. In plan-view foils produced this way, it was evident that some materials had been preferentially removed leaving behind a porous remnant. Despite the artefact, this type of foil offered the advantage that the oxidised β-Zr regions could be easily located and the oxidation product of the ω-phase could be investigated by a comparison with foils prepared electrolytically to remove the metal.

When the oxidised β-Zr region as a whole was brought into contrast, the region typically exhibited a contrast indicative of a fine grain structure, see for example Fig. 8(a). Imaging in the dark field mode confirmed that the grains were orientation related and that the grain size was on the nanometer scale. Microdiffraction patterns obtained from these fine grains were consistent with monoclinic ZrO_2. Since the oxidised β-Zr region was in the partially decomposed state prior to oxidation, a likely explanation would be that the observed monoclinic ZrO_2 arose from the oxidation of the Nb-depleted ω-phase, similar to the formation of ZrO_2 from the Nb-depleted α-Zr. Such an interpretation was confirmed by examining interfacial plan-view foils prepared by a chemical removal of the metal. The example shown in Fig. 10 was taken from an oxide formed during exposure to lithiated water for 176 days at 583 K following a pre-exposure of 350 h at 673 K in steam. Similar observations were obtained in oxides formed under other conditions. In Fig. 10, the grain structure within the oxidised β-Zr region resembled that of the ω-phase in the alloy and is easily distinguished from the coarser ZrO_2 grains oxidised from the adjacent α-Zr. A monoclinic ZrO_2 crystal structure for these fine grains was confirmed using microdiffraction and lattice imaging. EDX analyses, Fig. 9(b), showed that the Nb concentration for the fine-grained ZrO_2 was slightly higher than the surrounding ZrO_2, though significantly lower than the 20% for the β-Zr. Comparisons with EDX results from cross-sectional foils or plan-view foils prepared using electropolishing to remove the metal showed that Nb and Fe have been preferentially removed during the chemical thinning stage of foil preparation. The level of Nb and the lack of Fe in Fig. 9(b) are consistent with the ω-phase in the metal [29]. The morphological, structural and chemical information thus led to the conclusion that ω-phase oxidised to form monoclinic ZrO_2, and that the monoclinic ZrO_2 observed in the oxidised β-regions in cross-section foils was from the oxidation of the ω-phase.

3.4. Distribution of Fe

Fe has been found to be associated with the oxidised β-regions. In oxides containing partially decomposed β-Zr, the level of Fe detected varied with the location within the oxidised β-Zr. A location that consistently yielded a significant amount of Fe (and higher Nb) was the interface between the oxidised α-Zr and β-Zr. Fig. 8(c) compares the interface between the oxidised β-Zr and ZrO_2 with the adjacent locations. In oxides containing β-Nb initially, a partitioning of Fe to the interface between the oxidised α-Zr and oxidised β-Nb (in the amorphous form or as the sub-oxide) was evident when the interface could be manipulated to the edge-on orientation. However, there was considerable variation in the level of Fe in the oxidised β-Nb away from the interface with the ZrO_2. Some analyses of oxidised β-Nb showed Fe levels below the detection limit, while others showed detectable amounts of Fe. Such a variation remains consistent with a preferential segregation of Fe to the oxidised α/β interfaces, since the interfaces are generally non-planar and the overlap of the α/β regions cannot be avoided in all cases. The significance of the present observations is that the distribution of Fe in the oxide is similar to that in the alloy.

4. Discussion

4.1. Origin of image contrast in the SEM

The SEM image contrast described in Section 3.1.1 is unusual in that the secondary electron images exhibited significant variations with the accelerating voltage. In other words, the observed images contained information generated from a sub-surface region. In comparison, conventional secondary electron images convey information on the surface topography, as the contributing secondary electrons are generally emitted from the surface region of the sample.

The contrast can be interpreted based on the variations in the local surface charge, since deposition of a thin Au coating eliminated the contrast. The image contrast mechanism is similar to the field effect or voltage contrast commonly used in the characterisation of semiconductor devices [30,31]. In the SEM, secondary electrons are generally attracted to the detector by a potential field between the sample at ground potential and a positively biased Faraday cage a few centimetres away [30,31]. In the presence of a non-uniform

distribution of surface charge, the initial trajectories of secondary electrons leaving the sample are affected to different extents depending on the local field, Fig. 1(e). When a bias voltage is present, the variation of the surface charge with position may be obscured by the high collection efficiency. In the absence of a bias voltage, i.e. in the no-bias mode, only those secondary electrons leaving the vicinity of the sample with a direct line of sight to the detector are available for imaging, Fig. 1(e), and the variation of the surface charge with position can be revealed.

The transfer of the potential difference within the oxide to the sample surface can be understood from the semiconducting nature of ZrO_2, which can result in limited conductivity due to the generation of electron-hole pairs by the incident electrons. The interaction of electron-hole pairs with the local potential fields within the oxide can then lead to transfer of the sub-surface charge to the sample surface, Fig. 1(e). The distribution of charge at the sample surface thus represents a projection of the oxidised β-Zr regions within a thin slab of oxide penetrated by the incident electrons as illustrated in Fig. 1(e). The variation between images obtained at different voltages, Fig. 1(a)–(d), is therefore related to the microstructure within the oxide. In the present Zr–2.5Nb oxide, the overlap of the oxidised β-Zr appeared to be substantial at about 10 keV. The estimated penetration depth [30,31] for 10 keV electrons in ZrO_2 is about 0.5 μm, which is consistent with the typical grain depth of 0.3–0.5 μm and a Pilling–Bedworth ratio of 1.56.

4.2. Dual α/β phase structure and oxidation

The present work has applied SEM, TEM, EDX and EELS to the investigation of oxidised Zr–2.5Nb samples grown under various conditions (at 673 K or below in steam or in lithiated water environments). The observations made using both SEM and TEM have shown that the oxidised β-regions (β-Zr, ω + Nb enriched β-Zr and β-Nb) can be distinguished from the oxidised α-Zr regions (ZrO_2). In the SEM, the oxidised β-Zr regions are revealed via a combination of charge transfer and field effect contrast. The TEM examination of oxides in both cross-sectional and plan-view orientations provided a more direct imaging of the oxidised β-regions. The EDX microanalyses of the oxidised β-regions in suitably prepared foils have consistently shown the presence of Nb. Equally significant were the microanalyses that showed no discernible differences in the Nb content due to the conversion of α-Zr into ZrO_2.

The microstructural and microchemical observations lead to a general conclusion that, during the oxidation of Zr–2.5Nb, there is a correspondence between the oxide and the metal microstructures with respect to the dual α/β phases. The overall distribution of Nb in the oxide reflected the distribution associated with the α/β structure in the alloy. The detailed microstructure of the oxidised β-phases depended on the state of β-Zr decomposition at the time of oxidation (see Section 4.3). Such a correspondence is in accord with the low Nb mobility in the oxide at the oxidation temperature [32]. The identification of oxidised β-regions as distinct from ZrO_2 oxidised from α-Zr is also consistent with recent observations on the influence of morphology of β-Zr on the percentage hydrogen pickup [33]. Since Zr–2.5Nb pressure tube material has a highly anisotropic microstructure, the morphology of β-Zr relative to the oxidation surface can be varied by suitable sectioning of the pressure tube. A response of hydrogen pickup to variations in β-Zr morphology and its degree of decomposition prior to oxidation, demonstrates a corresponding variation within the oxide [33].

The distribution of Fe in the oxides examined here is also consistent with the retention of the dual phase structure in the oxide. In the alloy, Fe has been reported to be associated with the β-regions, the α–β interfaces and the α–α boundaries [26,29,34,35]. Our results show that Fe remained associated with the oxidised β-regions or the interface with ZrO_2 in the oxide. Information regarding Fe at oxidised α-α boundaries in the oxide is not available, since such locations cannot be readily identified in the oxide. The behaviour of Fe in Zr–2.5Nb can be compared with the behaviour of Fe in the oxidation of $Zr(Fe,Cr)_2$ intermetallics in Zircaloy-4 [36]. In Zircaloy-4, the Fe associated with the intermetallic precipitates remained localised upon initial incorporation into the oxide, but may be dissolved into the ZrO_2 matrix eventually [36]. Present results indicate that Fe remained localised to the oxidised β-regions in the oxides. A dispersal of Fe from the oxidised β-Zr or β-Nb, similar to the process in Zircaloy-4, may occur upon prolonged oxidation of Zr–2.5Nb; however, thicker oxides need to be examined for confirmation.

4.3. Decomposition of β-Zr and oxidation products

Based on observations on Zr–2.5Nb and Zr–20Nb oxides presented above, a general scheme can be derived for the oxidation of β-Zr which undergoes decomposition. The following are to be considered: the initial metastable β-Zr, the eventual equilibrium β-Nb and the intermediate ω-phase and Nb-enriched β-Zr [1]. Of these, the present results show that the Nb-depleted ω-phase oxidised to form monoclinic ZrO_2. For the Nb-enriched β-phases, the behaviours of β-Zr and β-Nb represented two extremes. In the case of β-Zr, a $Nb_2Zr_{x-2}O_{2x+1}$ oxide is formed, while β-Nb, when fully oxidised, formed an amorphous Nb-enriched oxide, presumably based on Nb_2O_5. The intermediate regime of Nb-enriched β-Zr is expected to follow the behaviour of either β-Zr or β-Nb depending on the Nb concentration.

The structure of $Nb_2Zr_{x-2}O_{2x+1}$ can be regarded as a modulated superstructure made up from subcells of metal and oxygen atoms [18–20]. The superstructure is incommensurate in nature in the sense that x is not restricted to being an integer, but is related to the Zr–Nb composition. An interesting feature of $Nb_2Zr_{x-2}O_{2x+1}$ is the ability to accommodate variations in the Nb concentration. For β-Zr in Zr–2.5Nb, it is expected that the $Nb_2Zr_{x-2}O_{2x+1}$ formed will have changing values of x in accordance with the Nb concentration in the Nb-enriched β-Zr as the decomposition proceeded. The range of x in $Nb_2Zr_{x-2}O_{2x+1}$ investigated by Thompson, Withers and co-workers [18–20] was between 7.1 and 12.0, corresponding to 28.5 and 16.9 wt%Nb. The exact range for the existence for $Nb_2Zr_{x-2}O_{2x+1}$ may be broader. However, it is not clear what the limiting composition is, at which the behaviour of Nb-enriched β-Zr switches to that of β-Nb in terms of forming an amorphous oxide.

The $Nb_2Zr_{x-2}O_{2x+1}$ is quite different from the common polymorphs of ZrO_2, specifically, the tetragonal form that can be present in small quantities in the primarily monoclinic ZrO_2 corrosion oxides films [3–20]. Spatially, $Nb_2Zr_{x-2}O_{2x+1}$ in Zr–2.5Nb pressure tube materials is formed from the oxidation of β-Zr. In comparison, the tetragonal ZrO_2 in Zr–2.5Nb oxide films has been shown, using a combination of Raman spectroscopy, X-ray texture measurements and electron microscopy [6,37–39], to be primarily associated with the monoclinic ZrO_2 [0 0 1] growth that developed over suitably oriented α-Zr grains. Structurally, the present electron diffraction results and previous Raman spectroscopy results [16] show that the structure of $Nb_2Zr_{x-2}O_{2x+1}$ formed from the β-Zr in Zr–20Nb alloy is distinct from ZrO_2. The main structural characteristics of $Nb_2Zr_{x-2}O_{2x+1}$ include the lack of distinct metal–oxygen distances and the metal–atom co-ordination number varying between 7 and 8 for a 0.26 nm limit of Zr–O bond [20]. It is suggested that the structural difference between $Nb_2Zr_{x-2}O_{2x+1}$ and ZrO_2 is related to differences in electrical properties and provides a basis for explaining the unusual SEM contrast from oxidised β-Zr in Zr–2.5Nb.

The observations of an amorphous oxide based on β-Nb at temperatures of 673 K and below are consistent with the oxidation behaviour for Nb and can be rationalised in terms of the mobilities of Nb and O in the oxide. It has been proposed [32] that the condition for forming an amorphous phase from the reaction of two species was for one species to have a high mobility while the other to have a low mobility in the product phase. The work of Thomas et al. [32] demonstrated that amorphous Nb and Ta oxides were formed at temperatures below 773 K and that crystallisation occurred when the mobility of the metallic species was increased at temperatures above 773 K.

The formation of an initial sub-oxide followed by an amorphous β-Nb based oxide indicates a delayed oxidation process with respect to α-Zr. Such a delayed oxidation is consistent with Zr having a higher affinity for oxygen than Nb. The preferential oxidation of Zr in Zr–Nb alloy resembles the preferential oxidation of Zr relative to the other (more noble) elements in the intermetallic precipitates in Zircaloy [36,40]. There is additional similarity in that the intermetallic precipitates also oxidised eventually to an amorphous state. In Zr–Nb alloys, the preferential formation of ZrO_2 has been reported [41] at oxidation temperatures considerably higher than used in the present work where the cations have higher diffusivities.

4.4. Influence on corrosion and hydrogen pickup behaviour

The corrosion behaviour of Zr–Nb alloys is affected by changes in the alloy microstructure. In the Zr–2.5Nb alloy, one beneficial effect is related to the reduction of Nb content in the α-Zr associated with the precipitation of β-Nb particles from supersaturated α-Zr either in materials quenched from the solution anneal temperature or in materials that were neutron or electron irradiated [42–47]. In the absence of irradiation, the corrosion response of Zr–2.5Nb improved due to the decomposition of β-Zr [33,42]. Recent results have shown that the corrosion resistance of Zr–2.5Nb pressure tube material was inferior when undecomposed β-Zr was aligned perpendicular to the oxide surface and that heat treatments used to improve the corrosion resistance affected the decomposition of the β-Zr without introducing detectable changes to the Nb content in the α-Zr [33]. For the Zr–20Nb alloy, the corrosion rate of the single phase β-Zr alloy is initially high but is reduced with the decomposition of β-Zr during the corrosion exposure [13]. Since the growth of Zr oxides is controlled by the inwards diffusion of oxygen, it follows that the difference in corrosion performances between materials containing differently decomposed β-Zr was related to the differences in the corrosion products. The formation of $Nb_2Zr_{x-2}O_{2x+1}$, which is structurally distinct from ZrO_2, in Zr–2.5Nb and Zr–20Nb alloys can be identified with the poor corrosion resistance of the alloys containing undecomposed β-Zr. The main implication is that $Nb_2Zr_{x-2}O_{2x+1}$ is a more effective diffusion medium for the supply of oxidants than ZrO_2.

With respect to hydrogen pickup, recent results have shown that hydrogen pickup can be reduced when the β-Zr was in a decomposed state prior to the corrosion exposure [33,42], and that the improvement was most effective when the β-Zr was aligned perpendicular to the oxide surface [33]. The formation of different oxidation products for β-Nb compared with β-Zr described above may be related to the greater reduction of hydrogen pickup in materials containing β-Nb compared with

materials containing β-Zr [33,42]. However, a mechanism for hydrogen pickup is currently lacking that would take into account the dependency on the morphology of the β-phase as well as the Nb concentration and the crystal structure of the oxidised β-regions.

5. Conclusions

The presence of oxidised β-Zr and related regions in oxides of Zr–2.5Nb can be identified using a number of electron microscopy and microanalysis techniques. In the SEM, the oxidised β-Zr regions in Zr–2.5Nb were imaged via a mechanism involving a combination of charge transfer and field effect contrast. Using the TEM, the presence of Nb in oxidised β-regions in suitably prepared foils was consistently demonstrated using EDX microanalyses. Fe was found to be associated with the oxidised β-regions and the distribution of Fe in the oxide was consistent with that in the alloy. The Nb concentration in ZrO_2 exhibited no discernible difference when compared with that of α-Zr from which the ZrO_2 was formed. The microstructural and microchemical observations show that there is a correspondence between the oxide and the Zr–2.5Nb pressure tube microstructures in terms of the dual α/β phases.

The detailed microstructure of the oxidised β-phases in Zr–2.5Nb depended on the state of β-Zr decomposition (β-Zr, Nb-enriched β-Zr, ω-phase and β-Nb) at the time of oxidation. The behaviours for β-Zr and β-Nb represented two extremes. The metastable β-Zr oxidised to form a $Nb_2Zr_{x-2}O_{2x+1}$ oxide, which is structurally distinct from the monoclinic, tetragonal or cubic polymorphs of ZrO_2 and can accommodate varying levels of Nb concentrations. The β-Nb was found to exhibit a delayed oxidation behaviour with respect to α-Zr. The β-Nb ultimately oxidises to an amorphous oxide. Prior to full oxidation, a metallic sub-oxide based on oxygen-enriched β-Nb was observed. For the ω and Nb-enriched β-Zr phases in partially decomposed β-Zr, the Nb-depleted ω-phase oxidised to form monoclinic ZrO_2. For the Nb-enriched β-Zr, its oxidation behaviour followed the behaviour of either β-Zr or β-Nb depending on the Nb content.

Acknowledgements

The work on Zr–2.5Nb was funded by Ontario Hydro and CANDU Owners Group. The work on Zr–20Nb was funded by AECL and CANDU Owners Group. We thank J. DeLuca, A. Audet, L.G. Laurin and V.C. Ling for technical assistance. We also thank V.F. Urbanic for providing the Zr–20Nb oxide samples. Valuable discussions with V.F. Urbanic, V. Perovic and D.W. McComb are also gratefully acknowledged.

References

[1] B.A. Cheadle, S. Aldridge, J. Nucl. Mater. 47 (1973) 255.
[2] R.G. Fleck, E.G. Price, B.A. Cheadle, ASTM STP 824, in: Proceedings of the 6th International Symposium on Zirconium in the Nuclear Industry, Vancouver, BC, Canada, June 28–July 1, 1982, ASTM, Philadelphia, 1984, p. 88.
[3] J. Godlewski, J.P Gros, M. Lambertin, J.F. Wadier, H. Weidinger, ASTM STP 1132, in: Proceedings of the 9th International Symposium on Zirconium in the Nuclear Industry, Kobe, Japan, 5–8 November 1990, ASTM, Philadelphia, 1991, p. 416.
[4] F. Garzarolli, H. Seidel, R. Tricot, J.P. Gros, ASTM STP 1132, in: Proceedings of the 9th International Symposium on Zirconium in the Nuclear Industry, Kobe, Japan, 5–8 November 1990, ASTM, Philadelphia, 1991, p. 395.
[5] B. Wadman, Z. Lai, H. Andren, A. Nystrom, P. Rudling, H. Pattersson, ASTM STP 1245, in: Proceedings of the 10th International Symposium on Zirconium in the Nuclear Industry, Baltimore, MD, USA, 21–24 June 1993, ASTM, Philadelphia, 1994, p. 579.
[6] Y.P. Lin, O.T. Woo, D.J. Lockwood, Mater. Res. Soc. Symp. Proc. 343 (1994) 487.
[7] S.B. Newcomb, B.D. Warr, W.M. Stobbs, Inst. Phys. Conf. Ser. 119 (1991) 221.
[8] B.D. Warr, E.M. Rasile, A.M. Brennenstuhl, M.B. Elmoselhi, N.S. McIntyre, S.B. Newcomb, W.M. Stobbs, in: M.J. Bennett, G.W. Lorimer (Eds.), Microscopy of Oxidation, The Institute of Materials, London, 1991, p. 292.
[9] B.D. Warr, M.B. Elmoselhi, S.B. Newcomb, N.S. McIntyre, A.M. Brennenstuhl, P.C. Lichtenberger, ASTM STP 1132, in: Proceedings of the 9th International Symposium on Zirconium in the Nuclear Industry, Kobe, Japan, 5–8 November 1990, ASTM, Philadelphia, 1991, p. 740.
[10] S.B. Newcomb, B.D. Warr, W.M. Stobbs, Proc. 13th Int. Congress on Electron Microscopy, Paris, France, 17–22 July 1994, Les Editions de Physique, Les Ulis, 1994, p. 1103.
[11] B.D. Warr, S.B. Newcomb, W.M. Stobbs, Proc. XI European Congress on Electron Microscopy, Dublin, Ireland, 1996, published on CD-ROM.
[12] R.A. Ploc, S.B. Newcomb, in: S.B. Newcomb, J.A. Little (Eds.), Microscopy of Oxidation 3, The Institute of Materials, London, 1997, p. 475.
[13] V.F. Urbanic, P.K. Chan, D. Khatamian, O.T. Woo, ASTM STP 1245, in: Proceedings of the 10th International Symposium on Zirconium in the Nuclear Industry, Baltimore, MD, USA, 21–24 June 1993, ASTM, Philadelphia, 1994, p. 116.
[14] Y.P. Lin, in: S.B. Newcomb, J.A. Little (Eds.), Microscopy of Oxidation 3, The Institute of Materials, London, 1997, p. 462.
[15] Y.P. Lin, J. DeLuca, Microsc. Microanal. 3 (2) (1997) 781.
[16] O.T. Woo, D.J. Lockwood, Y.P. Lin, V.F. Urbanic, Mater. Res. Soc. Symp. Proc. 357 (1995) 219.
[17] O.T. Woo, Y.P. Lin, J. Nucl. Mater. 270 (1999) 376.
[18] J.G. Thompson, R.L. Withers, J. Sellar, P.J. Barlow, B.G. Hyde, J. Solid State Chem. 88 (1990) 465.
[19] R.L. Withers, J.G. Thompson, B.G. Hyde, Acta Crystallogr. B 47 (1991) 166.

[20] K. Futterer, S. Schmid, J.G. Thompson, R.L. Withers, N. Ishizawa, S. Kishimoto, Acta Crystallogr. B 51 (1995) 688.
[21] D.C. Joy, A.D. Romig, J.I. Goldstein, Principles of Analytical Electron Microscopy, Plenum, New York, 1986, p. 249.
[22] G. Brauer, H. Mueller, G. Kuehner, J. Less-Common Met. 4 (1962) 533.
[23] N. Norman, J. Less-Common Met. 4 (1962) 52.
[24] D.W. McComb, Physcal Rev. B 54 (1996) 7094.
[25] V.F. Urbanic, M. Griffiths, ASTM STP 1270, in: Proceedings of the 17th International Symposium on Effects of Radiation on Materials, Sun Valley, Idaho, 20–23 June 1994, ASTM, Philadelphia, 1996, p. 1088.
[26] A. Perovic, V. Perovic, G.C. Weatherley, G.R. Purdy, R.G. Fleck, J. Nucl. Mater. 199 (1993) 102.
[27] V. Perovic, A. Perovic, G.C. Weatherley, L.M. Brown, G.R. Purdy, R.G. Fleck, R.A. Holt, J. Nucl. Mater. 205 (1993) 251.
[28] C.E. Lundin, R.H. Cox, USAEC Report GEAP 4089 (1962) 9.
[29] V. Perovic, A. Perovic, G.C. Weatherly, G.R. Purdy, J. Nucl. Mater. 224 (1995) 93.
[30] J.I. Goldstein, H. Yakowitz, Practical Scanning Electron Microscopy, Plenum, New York, 1976.
[31] D.E. Newbury, D.C. Joy, P. Echlin, C.E. Fiori, J.I. Goldstein, Advanced Scanning Electron Microscopy and X-Ray Microanalysis, Plenum, New York, 1986.
[32] O. Thomas, F.M. D'Heurle, A. Charai, Philos. Mag. B 58 (1988) 529.
[33] Y.P. Lin, J. Deluca, J. Nucl. Mater. 256 (1999) 1.
[34] O.T. Woo, G.J.C. Carpenter, J.A. Sawicki, S.R. MacEwen, J. Nucl. Mater. 172 (1990) 71.
[35] M. Griffiths, C.K. Chow, C.E. Coleman, R.A. Holt, S. Sagat, V.F. Urbanic, ASTM STP 1175, in: Proceedings of the 16th International Symposium on Effects of Radiation on Materials, Aurora, CO, USA, 23–25 June 1992, ASTM, Philadelphia, 1993, p. 1077.
[36] D. Pecheuer, F. Lefebvre, A.T. Motta, C. Lemaignan, J. Nucl. Mater. 189 (1992) 318.
[37] M.G. Glavicic, J.A. Szpunar, Y.P. Lin, J. Nucl. Mater. 245 (1997) 147.
[38] Y.P. Lin, Microsc. Microanal. 3 (2) (1997) 779.
[39] V.Y. Gertsman, Y.P. Lin, A.P. Zhilyaev, J.A. Szpunar, Philos. Mag. A 79 (1999) 1567.
[40] E.R. Bradley, R.A. Perkins, IWGFPT/34, ISSN 1011-2766, in: Proceedings of the IAEA Technical Committee Meeting on Fundamental Aspects of Corrosion of Zirconium Base Alloy in Water Reactor Environments, Portland, September 1989, IAEA, Vienna, 1990, p. 1011.
[41] R.A. Rapp, Corrosion 21 (1965) 382.
[42] V.F. Urbanic, M. Griffiths, in: Proceedings of the 12th International Symposium on Zirconium in the Nuclear Industry, Toronto, Canada, June 1998, ASTM, Philadelphia, to be published as ASTM STP 1354.
[43] V.F. Urbanic, B.D. Warr, A. Manolescu, C.K. Chow, M.W. Shanahan, ASTM STP 1023, in: Proceedings of the 8th International Symposium on Zirconium in the Nuclear Industry, San Diego, CA, USA, 19–23 June 1988, ASTM, Philadelphia, 1989, p. 20.
[44] K.N. Choo, Y.H. Kang, S.I. Pyun, V.F. Urbanic, J. Nucl. Mater. 209 (1994) 226.
[45] A.J.G. Maroto, R. Bordoni, M. Villegas, A.M. Olmedo, M.A. Blesa, A. Iglesias, P. Koenig, J. Nucl. Mater. 229 (1996) 79.
[46] V.F. Urbanic, J.E. LeSurf, A.B. Johnson, Corrosion 31 (1975) 15.
[47] O.T. Woo, G.M. McDougall, R.M. Hutcheon, V.F. Urbanic, M. Griffiths, C.E. Coleman, in: Proceedings of the 12th International Symposium on Zirconium in the Nuclear Industry, Toronto, Canada, June, 1998, ASTM, Philadelphia, to be published as ASTM STP 1354.